

Emergent Rashba spin-orbit coupling in bulk gold with buried network of nanoscale interfaces

Shreya Kumbhakar^{1,†,*}, Banashree Debnath^{1,†,*}, Tuhin Kumar Maji¹, Binita

Tongbram¹, Shinjan Mandal¹, T. Phanindra Sai¹, T.V. Ramakrishnan¹,

Manish Jain¹, H. R. Krishnamurthy^{1,2}, Anshu Pandey³, and Arindam Ghosh^{1,*}

¹*Department of Physics, Indian Institute of Science, Bangalore 560012, India*

³*Solid State and Structural Chemistry Unit, Indian Institute of Science, Bangalore 560012, India and*

²*International Centre for Theoretical Sciences, Tata Institute of Fundamental Research, Bangalore 560089, India*

The Rashba effect, which plays a crucial role in fundamental materials physics and potential spintronics applications, has been engineered in diverse systems, including semiconductor quantum wells, oxide heterostructures, metallic surfaces, topological insulators, ferroelectrics, etc. However, generating it in systems that preserve bulk inversion symmetry (BIS), for example, in bulk metals, has not been possible so far. We demonstrate a unique strategy to introduce and tune Rashba spin-orbit interaction (SOI) to unprecedented magnitudes in inversion-symmetric solids, by incorporating ultra-small silver nanoparticles in bulk gold. The near-identical lattice constants of Ag and Au allowed dense packing of the Ag/Au hetero-interfaces without compromising the global BIS. By varying the density of embedded nanoparticles, we generate Rashba SOI in a bulk metal with coupling strength ~ 15 meV.Å, higher than any known system preserving BIS globally and up to ~ 20 times increase in the spin-orbit scattering rate. We argue that the combined effect of charge-transfer at the interfaces and polaronic localization enhances the SOI.

Introduction

Materials lacking inversion symmetry exhibit Dresselhaus or Rashba spin-orbit coupling (SOC), which lifts the spin degeneracy of the bands without an external magnetic field. Bulk inversion asymmetry (BIA) in three-dimensional bulk periodic solids, like non-centrosymmetric zinc-blende structures, leads to the Dresselhaus SOC [1], whereas Rashba SOC emerges from structural inversion asymmetry (SIA), like in two-dimensional surfaces or interfaces [2, 3]. Intensive efforts have been employed over several decades to engineer artificial heterostructures from metals, semimetals, semiconductors, and insulators that show Rashba coupling [3, 4], which is modelled by the Bychkov-Rashba Hamiltonian $H_R = \alpha_R \vec{\sigma} \cdot (\vec{k} \times \hat{z})$. Here, $\vec{\sigma}$ and \vec{k} are the electron's spin and wavevector, respectively; α_R is the Rashba parameter, and \hat{z} is a unit vector along the direction of SIA *i.e.* perpendicular to the surface/interface. The magnitude of α_R ranges from $\sim 4 - 6$ meV.Å in III-V semiconductor quantum wells [5, 6] to $\sim 10 - 50$ meV.Å in interfaces of complex oxides heterostructures [7, 8] to $\sim 30 - 3000$ meV.Å on metallic surfaces or interfaces [9–12]. An ongoing quest over the years is the search for materials showing *bulk* Rashba effect, which had been mostly associated with 2D surfaces or interfaces [4, 13]. This was encouraged after the discovery of giant bulk Rashba splitting in polar semiconductors like BiTeX (X=Br, Cl, or I) [14–16], GeTe, SnTe, and organometal halide perovskites [17]. However, bulk systems showing the Rashba effect discovered so far lack a centre of inversion globally possessing a non-centrosymmetric structure and hence are observed in a restricted material domain [13]. Because of intrinsic structural symmetry, the Rashba interaction is absent in most metals, which are important for numerous spin-

manipulation-related applications [18–21]. This poses a fundamental question of whether it is possible to induce Rashba physics in a bulk system with global inversion symmetry.

Fundamentally, the Rashba interaction derives from the electric field associated with an interfacial potential gradient that is transformed to a magnetic field, which relativistically couples to the electron's spin. The utilization of interfaces has hence been a potential strategy to induce the Rashba effect. This has been demonstrated even on a metallic platform, where a non-centrosymmetric artificial superlattice of [Pt/W/Co] $_N$ ($N = 10$) enables Rashba physics in bulk metallic systems [22], with α_R as large as ~ 12 meV.Å. However, not only is the α_R strictly limited by the thickness of the metallic layers, but also its scalability to the bulk limit (*i.e.* large N) is experimentally challenging and yet to be demonstrated. Consequently, engineering the Rashba effect in a truly bulk metal that also preserves the bulk inversion symmetry remains unresolved.

In this work, we fabricate a crystalline matrix of Au that encloses multiple ultra-small Ag nanoparticles of diameter ~ 2 nm [23]. By performing quantum transport measurements, we show that the hybrid system exhibits a Rashba SOC with $\alpha_R \sim 15$ meV.Å. Our experiments suggest that this effect arises from the breaking of structural inversion symmetry and the strong dipole field generated locally at the Ag/Au interfaces because of the difference in the onsite electrochemical potentials of Au and Ag, which also leads to strong effective electron-phonon coupling [24], as well as a soft energy gap in the electronic spectrum at low energies. The Rashba coupling could be tuned over a factor of ~ 20 by varying the density of nanoparticles, thereby demonstrating a novel strategy to achieve tunable Rashba interaction in a bulk noble metal

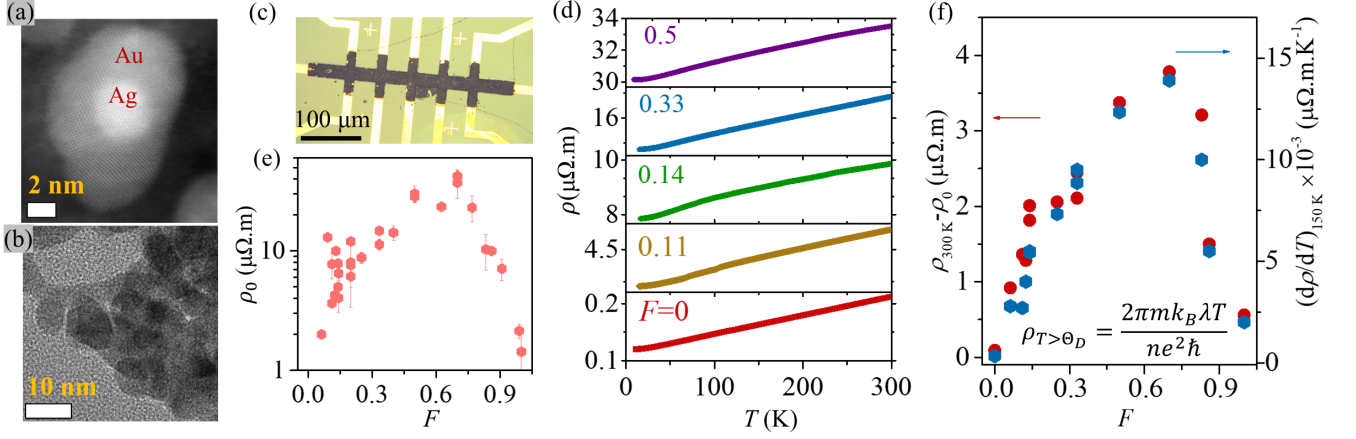


FIG. 1. Structural and electrical characterization of Ag@Au nanohybrid films: (a) z-contrast variation in High-Angle Annular Dark-Field imaging (HAADF) of Ag@Au nanohybrid indicates a spherical Ag nanoparticle (~ 2 nm dia), represented by the brighter white region, is hosted inside the Au lattice, represented by the darker grey region. (b) A High-Resolution Transmission Electron Microscopy (HRTEM) image shows multiple Ag nanoparticles (AgNPs) of high crystallinity embedded inside a crystalline matrix of Au. (c) shows the typical image of a film, represented by the darker region deposited on pre-patterned Cr/Au electrodes on a glass substrate, indicated by gold-coloured regions. (d) T -dependence of resistivity, ρ for films with varying Ag-Au volume fraction, $F = V_{\text{Ag}}/(V_{\text{Ag}} + V_{\text{Au}})$. (e) Variation of the residual resistivity, ρ_0 (defined as the resistivity, ρ at the base temperature $T \sim 6$ K) with F . (f) The T -dependent component of resistivity, $\rho_{300\text{ K}} - \rho_0$, and the slope of $\rho - T$ at $T \sim 150$ K are plotted in the left and right axes, respectively, for different values of F .

by embedding a network of nanoscale interfaces.

Results

Structural characterization

The Ag@Au nanohybrids are synthesized with a colloidal co-precipitation process [23, 24] that allows exceptional tunability in the density of the Ag/Au interfaces while retaining a global inversion symmetry owing to the near-perfect lattice matching of Ag and Au. (See Supplementary Information (SI) Section I for the details on synthesis, which are reproduced following references [23, 24]). Fig. 1(a) shows a typical z-contrast of a High-angle annular dark-field (HAADF) image of the Ag@Au nanohybrid, where the darker crystalline region of Au hosts a dispersion of the brighter region of Ag of diameter ~ 2 nm. Fig. 1(b) shows the High-Resolution Transmission Electron Microscope (HRTEM) image of a section of the crystalline Au matrix embedding multiple Ag nanoparticles. [23, 24]. It is also important to note from the HRTEM image that the spherical nature of the AgNPs and the Ag/Au interface is retained in the embedded structure. (See SI Section II for HRTEM images at different values of F). Our synthesis protocol offers precise tunability over the average radii of the embedded Ag nanoparticles (AgNPs), r_{Ag} , and their volume fraction, $F = V_{\text{Ag}}/(V_{\text{Ag}} + V_{\text{Au}})$. For all measurements reported in this manuscript, r_{Ag} is fixed at ~ 1 nm. Hence, the Ag-filling fraction, F , is also proportional to the volume density, F/r_{Ag} , of the interfaces. The as-synthesized nanohybrids are then assembled on pre-patterned Cr/Au electrodes on a glass substrate with chemical ‘cross-linking’

protocols to form a film with average thickness ~ 3 μm for electrical transport measurements [23] (See details on film preparation in SI Section III). A typical optical image of a patterned film is shown in Fig. 1(c), where the dark region corresponds to the Ag@Au nanohybrids (NHs).

Temperature-dependent Resistivity measurements

We have performed four-probe resistance measurements to estimate the resistivity, ρ , of the films. Fig. 1(d) shows the temperature (T)-dependence of ρ for films with varying F . All the films are metallic down to $T \sim 6$ K, indicating the formation of a true metallic composite from the Ag@Au NH that is devoid of tunnel barrier or insulating chemical residues across the Ag/Au interfaces. Fig. 1(e) shows the residual resistivity, ρ_0 (ρ at temperature ~ 6 K) for different Ag@Au NH films. We observe ρ_0 to increase with increasing F , reaching ~ 30 $\mu\Omega\cdot\text{m}$ at $F \sim 0.7$, which is two orders of magnitude higher compared to that of pristine Au (~ 0.1 $\mu\Omega\cdot\text{m}$). Such a significant enhancement arises from the buried Ag/Au interfaces that form the dominant source of scatterers and increase the resistivity almost linearly with increasing interface density, F/r_{Ag} [23]. By increasing F further, ρ_0 decreases, approaching ~ 1 $\mu\Omega\cdot\text{m}$ for a pure Ag nanoparticle (AgNP) film ($F = 1$). Fig. 1(f) (left axis) plots the T -dependent component of resistivity, $\rho_{300\text{ K}} - \rho_0$, which represents the phonon contribution to resistivity with F . To understand if the strong enhancement in $\rho_{300\text{ K}} - \rho_0$ is due to an apparent enhancement in the electron-phonon coupling at intermediate values of F [24–26], we simultaneously show the derivative of $\rho(T)$ with T (taken at

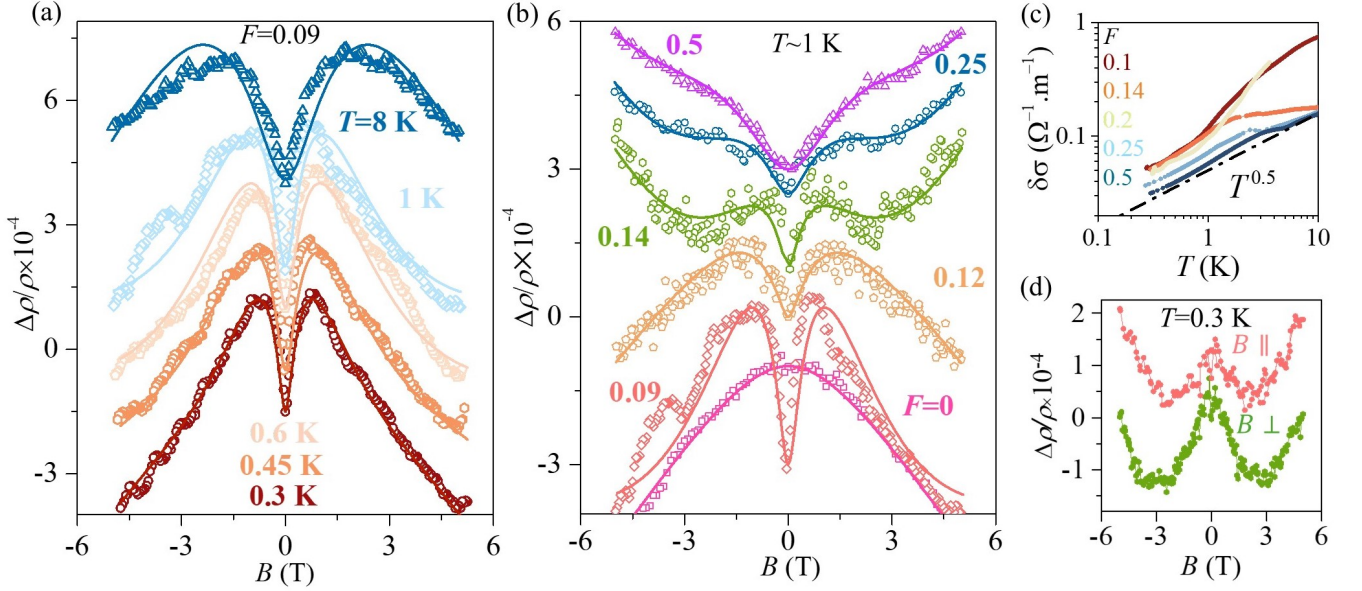


FIG. 2. Quantum transport: (a) Magnetoresistance (MR), represented by the relative change in resistivity $((\rho(B) - \rho(0))/\rho = \Delta\rho/\rho)$ with magnetic field (B), in a perpendicular magnetic field is measured for a film with Ag/Au interface density, $F = 0.09$ at the various temperatures indicated. (b) MR at $T \sim 1$ K is shown for different films with values of F varying from 0 to 0.5. $F = 0$ represents a pure Au nanoparticle film. All the data in (a) and (b) have been shifted vertically for visual clarity. Solid lines in (a) and (b) represent fits to the data using conductivity corrections from quantum interference and electron-electron interaction effects (Eq. [1]). (c) Low- T transport for different values of F is shown. This is quantified by the correction in conductivity, $\delta\sigma = -\delta\rho/\rho^2$, which is the change in conductivity ($\sigma = 1/\rho$) with respect to T , from its value at $T = 0$ K (σ_0), given by $\delta\sigma = \sigma - \sigma_0$. $\delta\rho$ indicates the change in ρ with respect to T . σ_0 is estimated by extrapolation of the data to $T = 0$. (d) MR, measured at $T = 0.3$ K, is shown for a film with $F = 0.14$ in magnetic fields applied parallel and perpendicular to the film.

$T \sim \Theta_D = 150$ K, where Θ_D is the Debye temperature) on the right axis of Fig. 1(f). Since $\rho \approx 2\pi m k_B \lambda T / \hbar n e^2$, where n and m are the electron's number density and mass, respectively, and λ is the electron-phonon coupling (EPC) constant [27], the slope of the $\rho - T$ curve directly corresponds to λ . The correspondence between $\rho_{300\text{ K}} - \rho_0$ and $d\rho/dT$ suggests strong effective EPC, enhanced by nearly ~ 100 times compared to that in bulk Ag or Au. Such an increase in EPC was recently suggested to arise from the charge transfer across Ag/Au interfaces [24, 25]. The impact of the interfaces and large EPC on the spin- and spin-orbit-related processes can be nontrivial, especially due to the breaking of structural inversion symmetry at the interfaces.

Magnetotransport measurements

To probe the SOC, we have performed magnetotransport measurements down to $T \sim 0.3$ K, with which we probe the phase-coherent processes and the spin-orbit scattering (See SI Section IV for details on the measurement). The magnetoresistance (MR) for a film, captured by $\Delta\rho/\rho$, with $F = 0.09$ is shown in Fig. 2(a) at T varying within 0.3 – 8 K. At all T , we observe the MR increases with magnetic fields (B) at lower B and then decreases at higher values of B . These represent the well-studied weak antilocalization (WAL) and weak

localization (WL) behaviours observed in disordered conductors at low temperatures due to quantum interference effects [28–32]. (See SI Section V-VI for results on other values of F). The probability of the interference thus depends on the phase-breaking timescale, τ_ϕ . The nature of localization, on the other hand, *i.e.* WL or WAL, is determined by the spin-orbit scattering time, τ_{soc} , which introduces a relative phase in the electronic wavefunctions. Specifically, positive MR or WAL emerges from higher SO scattering *i.e.* $\tau_{\text{soc}} < \tau_\phi$ and vice-versa. Interestingly, we observe from Fig. 2(a) that the WL component decreases with increasing T , whereas the WAL component is almost constant. While the former behaviour of MR indicates decreasing τ_ϕ with increasing T , which is generally observed across different systems, the latter dependence shows an unusual enhancement in the SOC with increasing T .

Fig. 2(b) shows the MR for films with different values of F at $T \sim 1$ K. For the pure Au nanoparticle (Au NP) film ($F = 0$), we observe negative MR throughout the entire B range, indicating WL. With increasing F , we find a distinct emergence of positive MR at low- B , suggesting WAL and, hence, enhanced SOC strength. Since Au, being heavier than Ag, has a higher intrinsic SOC [33], this increase of SOC with the incorporation of Ag in the hybrid system points toward an unconventional mechanism of spin-orbit scattering. We also observed another upturn in MR at higher magnetic fields for $F \gtrsim 0.12$,

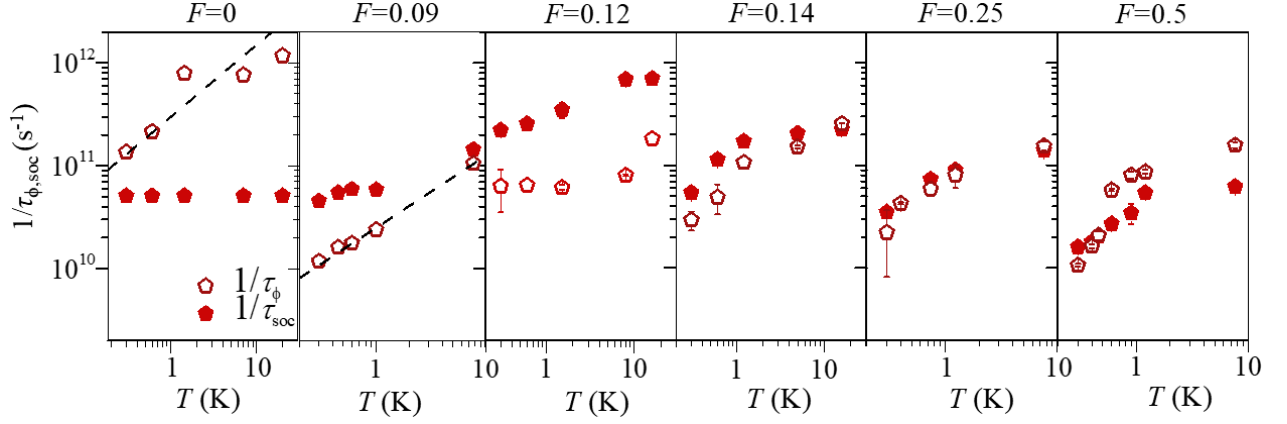


FIG. 3. **Phase-breaking and Spin-orbit interaction timescales:** Temperature (T)-dependences of spin-orbit interaction rate ($1/\tau_{\text{soc}}$) and phase-breaking rate ($1/\tau_{\phi}$) are shown for varying values of F . τ_{soc} and τ_{ϕ} are estimated from the fits to the quantum transport data, shown in Fig. 2(a) and 2(b) using Eq. [1]. The black dashed lines in the first two panels for $F = 0, 0.09$ represent $T^{-0.7}$ dependence of $1/\tau_{\phi}$.

which we attribute to the effects of the electron-electron interaction (EEI) [34, 35]. The proportionality of $\delta\sigma$ at low T with $T^{1/2}$, shown in Fig. 2(c) also suggests strong EEI with increasing F [34, 36].

To quantitatively estimate τ_{ϕ} and τ_{soc} , we have fitted the quantum transport data with additive conductivity corrections from WL/WAL and EEI effects [37, 38]. Since conductivity correction from EEI essentially arises from the Zeeman splitting of the spin levels, we have considered the Maekawa-Fukuyama form of WL/WAL [31]. Furthermore, we have considered a 3D model for both effects [32, 34, 35] since the MR in parallel and perpendicular fields are essentially the same, showing isotropic MR, as shown in Fig. 2(d). We fit the measured quantum correction to conductivity as follows.

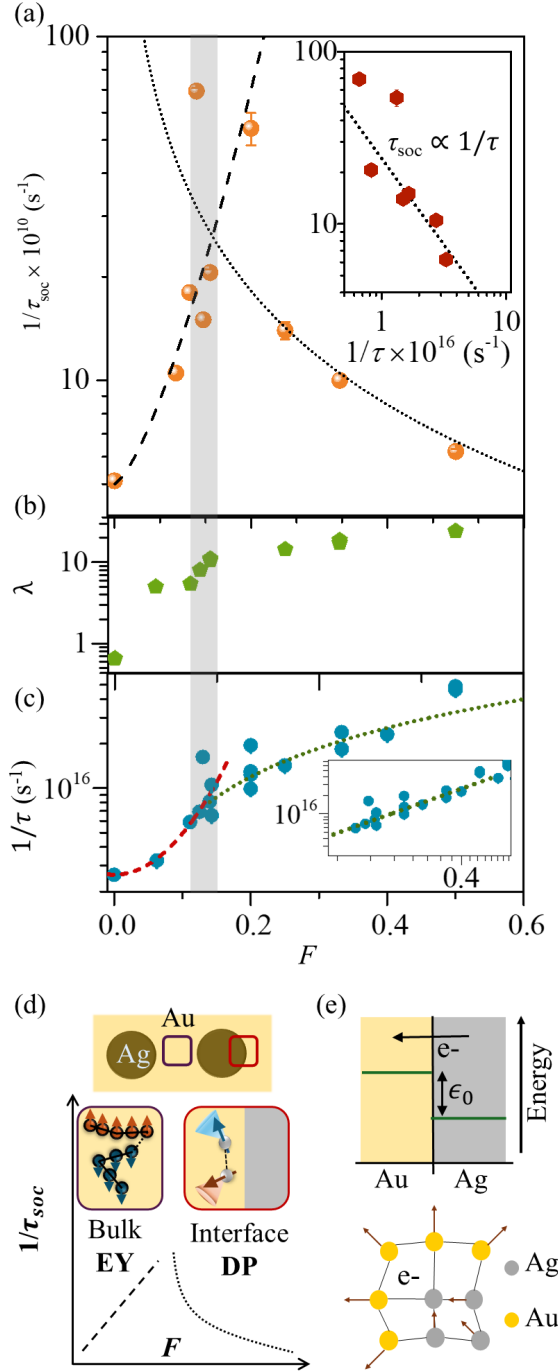
$$\frac{\Delta\rho}{\rho^2} = \frac{\Delta\rho}{\rho^2}\bigg|_{\text{QI}} + \frac{\Delta\rho}{\rho^2}\bigg|_{\text{EEI}} \quad (1)$$

Here, $\frac{\Delta\rho}{\rho^2}\bigg|_{\text{QI}}$ and $\frac{\Delta\rho}{\rho^2}\bigg|_{\text{EEI}}$ are the conductivity corrections from quantum interference and EEI effects, respectively. The analytical forms of the fit equation can be found in the **Materials and Methods** section. It is to be noted that the quantum interference effects *i.e.* WL/WAL and the EEI effects differ in T and B -dependences. While quantum interference gets suppressed with increasing T (Fig. 2a and SI Section V) as the dephasing rate of the electron increases, the magnetic field-dependent component of EEI enhances with T and always exhibits positive MR. Fits to the MR data using Eq. [1] with four fitting parameters B_{ϕ} , B_{soc} , g , and \mathcal{F}_{σ} are shown by the solid lines in Fig. 2(a),(b), where $B_{\phi} = \hbar/4eD\tau_{\phi}$ and $B_{\text{soc}} = \hbar/4eD\tau_{\text{soc}}$ are the scales of phase-breaking magnetic field and spin-orbit magnetic field, respectively, \mathcal{F}_{σ} is the average Coulomb interaction over the Fermi surface, and g is the Lande g -factor. [See SI section V-VI for details on the fits and fitting parameters at all values of F and T .] Diffusivity, $D = mv_F^2/3ne^2\rho$, that is dependent on F has been estimated from the measured

ρ , and constant number density, $n = 10^{28} \text{ m}^{-3}$, electronic mass, $m = 10^{-30} \text{ kg}$, and Fermi velocity of Au, $v_F = 1.4 \times 10^6 \text{ m.s}^{-1}$. (See SI Section IV for Hall measurements showing the estimation of n .)

Fig. 3 shows the T -dependence of τ_{ϕ} and τ_{soc} for different films with F ranging within 0 – 0.5. The T -dependence of τ_{ϕ} follows $\sim T^{-p}$ behaviour with $p \sim 0.7 - 1$ for lower Ag-filling ($F \lesssim 0.09$), indicating that electron-electron interaction likely dominates the phase-breaking mechanism [34]. With increasing F , the T -dependence of $1/\tau_{\phi}$ deviates from a pure power law, becoming the weakest for $F \sim 0.12 - 0.14$, which suggests strong modification of the phase-breaking processes. (See SI Section VI for results at other values of F). Secondly, the SO scattering rate, $1/\tau_{\text{soc}}$, first increases with increasing F as compared to that of pristine Au, until $F \sim 0.12$, after which it decreases again. We find this behaviour at all temperatures, indicating it to be related to the nanostructuring of Au. Finally, we find an emerging T -dependence in $1/\tau_{\text{soc}}$ at larger F , which again points towards an unconventional origin of SOC in the system, likely due to the presence of interfaces.

Fig. 4(a) shows the F -dependence of $1/\tau_{\text{soc}}$ (for $T \sim 8 \text{ K}$), where the nonmonotonicity of $1/\tau_{\text{soc}}$ in F is evident. $1/\tau_{\text{soc}}$ first increases with increasing F , reaching $\sim 7 \times 10^{11} \text{ s}^{-1}$ at $F = 0.12$, which is more than an order of magnitude larger compared to that of pure Au NP film ($1/\tau_{\text{soc}} \sim 5 \times 10^{10} \text{ s}^{-1}$). Further increase in F causes $1/\tau_{\text{soc}}$ to decrease, approaching $\sim 5.5 \times 10^{10} \text{ s}^{-1}$ at $F = 0.5$. Intriguingly, we find that both λ , estimated from the slope of $\rho - T$ in Fig. 1(f), and $1/\tau$ (calculated from the residual resistivity in Fig. 1(e)), undergo a change in their respective behaviour at very similar values of F . As shown in Fig. 4(b), λ increases sharply from ~ 0.6 at $F = 0$ to ~ 10 at $F = 0.14$, after which the increase in λ becomes weaker. Similarly, $1/\tau$ also increases in a super-linear manner with F until $F \sim 0.13$ (red dashed line), after which it becomes almost linear



(green dotted line, also in the double logarithmic plot in the inset of Fig. 4c). Since the linear increase in $1/\tau$ with F has been quantitatively shown to correspond to interface-dominated scattering [23], the nonmonotonic F -dependence of $1/\tau_{\text{soc}}$ seems to represent a crossover in the nature of transport at $F \sim 0.13$, from bulk disorder dominated to that determined by the buried Ag/Au interfaces.

Spin relaxation mechanisms are widely classified into two types (see the schematic of Fig. 4(d)). The first is the Elliot-Yafet (EY) mechanism [39, 40], where the conduc-

FIG. 4. Rashba spin-orbit coupling: (a) Top panel shows the variation of the spin-orbit scattering rate ($1/\tau_{\text{soc}}$) with F at $T \sim 8$ K. (b) shows electron-phonon coupling (EPC) constant (λ), estimated from $[\rho/\rho_0]_{150 \text{ K}}$ (Fig. 1(f)) at different values of F using the expression $\rho_{T > \Theta_D} = 2\pi\lambda m k_B T / ne^2 \hbar$. (c) plots the electron scattering rate ($1/\tau$), estimated from the residual resistivity, ρ_0 (Fig. 1(e)) using the Drude expression of resistivity. The dashed and dotted lines in (a) represent exponential and linear dependences on F , respectively. The linear dependence of $1/\tau$ on F is further illustrated in the inset of (c). The dashed and dotted lines in (a) represent $1/\tau_{\text{soc}} \propto 1/\tau$ and $1/\tau_{\text{soc}} \propto \tau$, respectively, with the expressions derived from the extrapolations of $1/\tau$ vs F in (c). The inset in (a) shows the proportionality of $1/\tau_{\text{soc}}$ with τ for $F \gtrsim 0.11$. $\alpha_R \approx 15 \text{ meV}\cdot\text{\AA}$ is estimated from the slope of the dotted line using the expression of DP spin relaxation, $\tau_{\text{soc}} = 3\hbar^4 / 8\alpha_R^2 m^2 v_F^2 \tau$. (d) Different mechanisms of spin relaxation are illustrated. At lower F , the EY mechanism originating from disorder potential in the bulk (purple box) dominates, whereas the DP mechanism from Rashba coupling at the interface (red box) is significant at higher- F . (e) (Top panel) A schematic of the electrochemical potential of electrons at the Ag and Au sites across the Ag@Au nanohybrid is shown, ϵ_0 being the potential difference between them. Electrons transfer from a higher onsite potential at Ag to a lower potential in Au. (Bottom panel) demonstrates the polaronic trapping of electrons at the Ag/Au interface.

tion electron spin interacts with its motion in the electric field of the host lattice described by the periodic potential. Here, spins of the conduction electrons relax/change due to momentum-scattering events that give rise to a spin-orbit scattering rate directly proportional to the momentum-scattering rate ($\tau_{\text{soc}} \propto \tau$). The other is the Dyakonov-Perel (DP) mechanism [41, 42], where inversion symmetry breaking from Rashba coupling leads to a momentum-dependent effective magnetic field, which causes spin precession and resultant dephasing. Momentum scattering, in this case, causes rapid fluctuations in the internal magnetic field and disruption of the spin dephasing. Thus, τ_{soc} induced by a Rashba interaction becomes longer as the electron scattering time, τ , becomes shorter ($\tau_{\text{soc}} \propto 1/\tau$). The inset of Fig. 4(a) shows the dependence of $1/\tau_{\text{soc}}$ on $1/\tau$, where $1/\tau$ is calculated from the magnitude of ρ_0 , consistent with the fitting of the MR data, for films with $F > 0.12$. The inverse relation (dotted line) indicates the DP-type spin relaxation, which is consistent with the possibility of structural symmetry breaking at the Ag/Au interfaces. The dotted line in Fig. 4(a) represents the same behavior by mapping $1/\tau$ onto F (green dotted lines in Fig. 4(c) and inset). Quantitatively, one expects $\tau_{\text{soc}} = 3\hbar^4 / 8\alpha_R^2 m^2 v_F^2 \tau$ in three dimensions, which yields $\alpha_R \approx 15 \text{ meV}\cdot\text{\AA}$ (dotted line in the inset of Fig. 4(a)). This is in close agreement with the Rashba interaction observed and computed at the planar interfaces created by depositing (few-layer) Ag on Au(111) substrate [43]. Finally, the dashed line describing the sharp increase in $1/\tau_{\text{soc}}$ at low F in Fig. 4(a) is representative of $\tau_{\text{soc}} \propto \tau$, *i.e.* the EY mechanism, obtained by empirically fitting the $1/\tau$ data to F at low

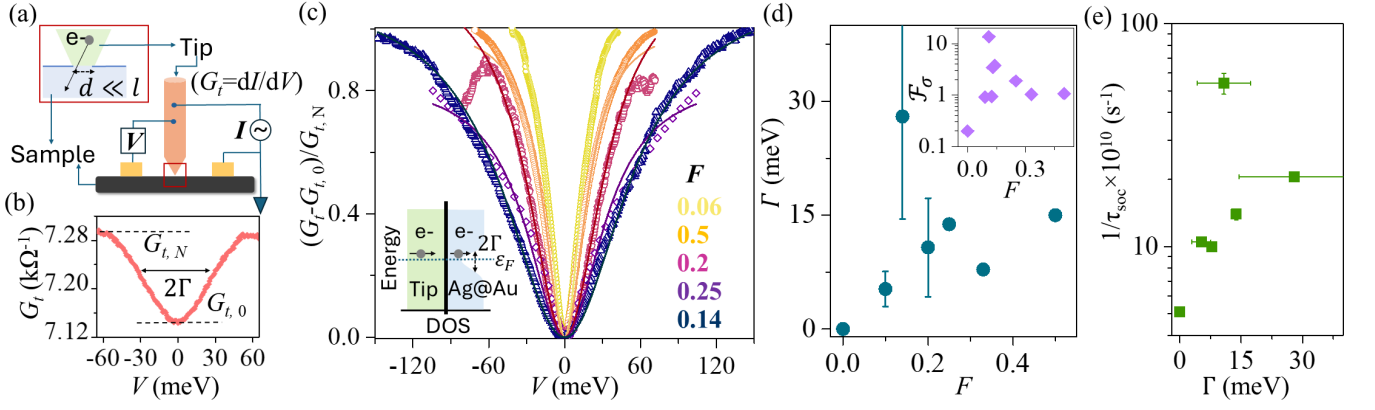


FIG. 5. Tunnelling measurements: (a) The schematic of the experimental set-up. The tip is biased with a voltage (V) while the sample is grounded, thereby driving a current (I) across the tip-sample nanocontact of dimension d and tunnelling conductance, $G_t = dI/dV$. (b) Typical G_t for a films with $F = 0.14$, measured at $T \sim 8$ K. (c) G_t is shown for different films with varying F , measured at $T \sim 8$ K. G_t is normalized such that the minimum value at zero bias, $G_{t,0}$ is 0 and the value saturating at larger bias, $G_{t,N}$ is 1. Solid lines are Lorentzian fits to the spectra with fitting parameter, Γ representing the width of *soft-gap* in the electronic DOS, illustrated schematically in the inset. (d) Variation of Γ with F is shown. Inset: \mathcal{F}_σ , representing the Coulomb screening parameter, estimated from quantum transport measurements. (e) Variation of $1/\tau_{\text{soc}}$ at $T \sim 8$ K with Γ measured for different films with varying F .

values ($F \lesssim 0.12$, red dashed line in Fig. 4(c)). Fig. 4(d) depicts the two regimes of spin-relaxation observed at different regimes of F . Fig. 4(e) illustrates two key physical phenomena that could be intimately linked to the breaking of structural inversion symmetry and origin of the Rashba coupling. The top panel shows the charge transfer at the Ag/Au interface, driven by the difference of onsite electrochemical potential (ϵ_0) (a theoretical estimation of the charge occupancy is shown in the SI section VII), and bottom panel demonstrates possible polaronic distortion at the interface, linked to the giant electron-phonon coupling reported in these structures [24].

Detailed studies have shown that large Rashba splitting is observed for surface states of noble metals like Au, Ag, and Cu [9, 10, 44–50] that are truly localized at the surface, and their asymmetric nature across the surface crucially determines the magnitude of the Rashba effect. This can be understood in a simple way by relating the gradient of the wave function to the electric field close to the atomic core, which leads to the momentum-dependent magnetic field $\sim (\vec{k} \times \hat{z})$ [47–50]. In fact, confinement of the electron gas close to the interface has been found to enhance Rashba splitting in oxide and semiconductor heterostructures as well [51]. Hence, the dominance of the Rashba effect with increasing interface density, F of the Ag@Au hybrid structure, could accompany increasing localization of electronic wave functions close to the interface with higher F .

Tunnelling measurements

We have probed the electronic density of states (DOS) by performing tunnelling measurements on the films [24, 52] to obtain evidence of such localization and its

connection with the SOC. The experimental schematic is illustrated in Fig. 5(a). A sharp metallic tip is brought in contact with the sample to measure the differential conductance ($G_t = dI/dV$) by passing a current, I , through the tip at a particular bias, V . The dimension of the tip-sample contact was kept low for conductance to probe the tunnelling density of states (DOS). Fig. 5(b) shows the G_t measured for a typical film of $F = 0.14$ while varying V within ± 60 meV at $T \sim 8$ K. We observe a conductance minimum ($G_{t,0}$) at zero bias, which increases and saturates at larger bias, denoted by $G_{t,N}$. The full-width half maximum of the dip in conductance, represented by Γ is ≈ 30 meV. Fig. 5(c) shows the normalized tunnelling spectra at $T \sim 8$ K measured for varying values of F . From the homogeneity of the dip across the film and its T -dependence (See SI Section VIII), we exclude possibilities of disorder/impurity-mediated tunnelling for the conductance minima and attribute this to opening of a *soft gap*, of width Γ , in the electronic DOS of the film, as represented schematically in the inset of Fig. 5(c). To extract Γ precisely, we have fitted the spectra with a Lorentzian curve. Fig. 5(d) shows the estimation of Γ at different values of F . We observe Γ increases with increasing F , reaching a maximum of ~ 30 meV close to $F \sim 0.14$, after which it decreases again. The inset shows that the Coulomb screening parameter, \mathcal{F}_σ , estimated from quantum transport measurements, reaches a pronounced maximum close to $F \sim 0.14$, where Γ is also the highest. This further suggests that there is a depletion of itinerant electrons at the Fermi level, which results in a reduction of the Coulomb screening and enhanced \mathcal{F}_σ .

Polaronic localization of electrons close to the Ag/Au interfaces, like in small polarons, can enhance the wave function asymmetry, thus making Rashba coupling the

dominant source of spin relaxation. Using both quantum transport and tunnelling measurements, we observe τ_{soc} and Γ to peak around $F \sim 0.14$, implying the highest probability of localization and resulting interface-dominated electrical transport and inversion symmetry-breaking. This is quantitatively captured by the direct correspondence between $1/\tau_{\text{soc}}$ and Γ in Fig. 5(e). It is possible that the T -dependence of $1/\tau_{\text{soc}}$ is also related to the temperature-driven dynamics of polarons, although further understanding is required.

Discussion

To summarize, we have demonstrated a novel metallic system where a Rashba SOC can be induced by a network of nanoscale interfaces. We show the coupling strength is tunable over an order of magnitude by varying the interface density (F), reaching a maximum value of ~ 15 meV.Å. We report, for the first time, Rashba coupling in a bulk metal that also globally preserves the inversion symmetry, though there is local inversion symmetry breaking by the buried interfaces. We have further demonstrated the crossover from EY-type to DP-type spin relaxation by tuning the interface density, which is usually difficult to achieve on the same material platform. We show a unique interplay of electron-phonon coupling and Rashba interaction that can lead to many-body quantum states like spin-orbital polarons [53].

Materials and Methods

Material synthesis:

Ag@Au nanohybrids were synthesized via a two-step colloidal process[23, 24]. First, AgNO_3 was reduced with ice-cold NaBH_4 in ultrapure water (~ 18.2 MΩ·cm) containing NaOH , NH_4Br , KI , and CTAB to form AgNPs. Then, HAuCl_4 was added at 40°C under stirring to form a gold shell. The reaction was monitored by UV-Vis spectroscopy and quenched with IPA, followed by centrifugation at 10,000 rpm for 30-45 minutes to remove excess CTAB.

The nanohybrids were drop-cast onto pre-patterned Cr/Au ($\sim 10/70$ nm) electrodes on glass. Samples were dissolved in CHCl_3 , dried at 60°C , and washed sequentially with DI water, KOH , and IPA to remove residual CTAB and promote sintering. This cycle was repeated ten times to form films of thickness, $t \approx 3 \pm 0.5 \mu\text{m}$ (See Fig. S2).

Electrical transport measurements:

Four-probe resistivity measurements of the Ag@Au nanohybrids were carried out in home-built cryostats down to ~ 6 K using a DC current of $\sim 100 \mu\text{A}$

sourced by a Keithley 6221, while the voltage was measured using a Keithley 2182A nanovoltmeter. A Keithley 3700 multiplexer card enabled voltage acquisition across multiple contact pairs. Delta-mode voltage measurement was used to suppress thermal electromotive force (thermo-EMF)(See SI section IV). For lower temperatures ($T \sim 10$ K to 0.3 K), resistivity and magnetotransport measurements were performed in a He-3 cryostat. The tunnelling measurements were performed in another home-built cryostat that can cool down to ~ 5 K and hosts a specialized tip-sample chamber with nanopositioners (attocubes and piezo tubes) connected to the tip holder, and electrical contacts attached to both the tip and the film. A sharp Pt/Rh metallic tip is brought in contact with the film in a controlled manner with the help of the nanopositioners as indicated in the schematic of the experimental set-up in Fig. 5(a) of main manuscript.

Analysis of quantum transport data:

Quantum transport data was analyzed using weak localization (WL), weak antilocalization (WAL), and electron-electron interaction (EEI) corrections to extract phase coherence time(τ_ϕ) and spin-orbit scattering time(τ_{soc}). The Maekawa-Fukuyama model was applied for WL/WAL effects, while a 3D model was used for both WL/WAL and EEI due to the isotropic magnetoresistance observed in the films. The conductivity corrections were then fitted to the experimental data. The total quantum correction to conductivity is shown in Eq. [1] of the main text. Here, $\frac{\Delta\rho}{\rho^2}\Big|_{\text{QI}}$ and $\frac{\Delta\rho}{\rho^2}\Big|_{\text{EEI}}$ are the conductivity corrections from quantum interference and EEI effects, respectively [29, 32].

1. Conductivity correction due to quantum interference:

$$\begin{aligned} \frac{\Delta\rho}{\rho^2}\Big|_{\text{QI}} = & \frac{e^2}{2\pi^2\hbar} \sqrt{\frac{eB}{\hbar}} \left[\frac{1}{2\sqrt{1-\gamma}} \left(f_3\left(\frac{B}{B_-}\right) - f_3\left(\frac{B}{B_+}\right) \right) \right. \\ & - f_3\left(\frac{B}{B_2}\right) - \sqrt{\frac{4B_{\text{soc}}}{3B}} \left\{ \frac{1}{\sqrt{1-\gamma}} (\sqrt{t_+} - \sqrt{t_-}) \right. \\ & \left. \left. + (\sqrt{t} + \sqrt{t+1}) \right\} \right] \end{aligned} \quad (2)$$

where

$$f_3(z) = \sum_{n=0}^{\infty} \left[2(\sqrt{n+1+z} - \sqrt{n+z}) - \frac{1}{n + \frac{1}{2} + z} \right] \quad (3)$$

Here, $B_\phi = \hbar/4eD\tau_\phi$ and $B_{\text{soc}} = \hbar/4eD\tau_{\text{soc}}$ are the scales of phase-breaking magnetic field and spin-orbit magnetic field, respectively. $t = 3B_\phi/4B_{\text{soc}}$

qualitatively represents the strength of WL to WAL, $\gamma = (3g^*\mu_B B/8eDB_{\text{soc}})^2$ represents the strength of Zeeman splitting where g^* is the effective g-factor. B_{\pm}, B_2 are characteristic fields given as: $B_{\pm} = B_{\phi} + \frac{2}{3}B_{\text{so}}(1 \pm \sqrt{1-\gamma})$, and $B_2 = B_{\phi} + \frac{4}{3}B_{\text{so}}$. It is to be noted that we have not considered any spin-flip scattering that can arise from magnetic impurities, thus implicitly making the phase-coherent and inelastic scattering processes equivalent *i.e.* $\tau_i = \tau_{\phi}$, τ_i being the inelastic scattering time.

2. Conductivity correction due to electron-electron interaction [34]:

$$\frac{\Delta\rho}{\rho^2}\bigg|_{\text{EEI}} = \frac{8e^2}{3\pi^2\hbar}\mathcal{F}_{\sigma}\left(\left(1 + \frac{\mathcal{F}_{\sigma}}{2}\right)^{3/2} - 1 - \frac{3\mathcal{F}_{\sigma}}{4}\right) \times \sqrt{\frac{T}{2D}}g_3(h) \quad (4)$$

where

$$\mathcal{F}_{\sigma} = \frac{\int d\hat{\Omega}v(q=2k_F\sin(\theta/2))}{\int d\hat{\Omega}v(0)} \quad (5)$$

is the average of the Coulomb interaction $v(q)$ on the Fermi surface over the solid angle $\hat{\Omega}$.

[†]**Equal contribution**

***Corresponding authors:**

shreyak@iisc.ac.in

banashreed@iisc.ac.in

arindam@iisc.ac.in

-
- [1] Dresselhaus, G. Spin-Orbit Coupling Effects in Zinc Blende Structures. *Phys. Rev.* **1955**, *100*, 580–586.
 - [2] Bychkov, Y. A.; Rashba, É. I. Properties of a 2D electron gas with lifted spectral degeneracy. *Soviet Journal of Experimental and Theoretical Physics Letters* **1984**, *39*, 78.
 - [3] Manchon, A.; Koo, H. C.; Nitta, J.; Frolov, S. M.; Duine, R. A. New perspectives for Rashba spin-orbit coupling. *Nature materials* **2015**, *14*, 871–882.
 - [4] Bihlmayer, G.; Noël, P.; Vyalikh, D. V.; Chulkov, E. V.; Manchon, A. Rashba-like physics in condensed matter. *Nature Reviews Physics* **2022**, *4*, 642–659.
 - [5] Schmult, S.; Manfra, M. J.; Punnoose, A.; Sergent, A. M.; Baldwin, K. W.; Molnar, R. J. Large Bychkov-Rashba spin-orbit coupling in high-mobility GaN/Al_xGa_{1-x}N heterostructures. *Phys. Rev. B* **2006**, *74*, 033302.
 - [6] Stefanowicz, W.; Adhikari, R.; Andrearczyk, T.; Faina, B.; Sawicki, M.; Majewski, J. A.; Dietl, T.; Bonanni, A. Experimental determination of Rashba spin-orbit coupling in wurtzite *n*-GaN:Si. *Phys. Rev. B* **2014**, *89*, 205201.
 - [7] Caviglia, A. D.; Gabay, M.; Gariglio, S.; Reyren, N.; Cancellieri, C.; Triscone, J.-M. Tunable Rashba Spin-Orbit Interaction at Oxide Interfaces. *Phys. Rev. Lett.* **2010**, *104*, 126803.
 - [8] Lin, W.; Li, L.; Doğan, F.; Li, C.; Rotella, H.; Yu, X.; Zhang, B.; Li, Y.; Lew, W. S.; Wang, S.; others Interface-based tuning of Rashba spin-orbit interaction in asymmetric oxide heterostructures with 3 d electrons. *Nature communications* **2019**, *10*, 3052.
 - [9] LaShell, S.; McDougall, B. A.; Jensen, E. Spin Splitting of an Au(111) Surface State Band Observed with Angle Resolved Photoelectron Spectroscopy. *Phys. Rev. Lett.* **1996**, *77*, 3419–3422.
 - [10] Mugarza, A.; Mascaraque, A.; Repain, V.; Rousset, S.; Altmann, K. N.; Himpsel, F. J.; Koroteev, Y. M.; Chulkov, E. V.; García de Abajo, F. J.; Ortega, J. E. Lateral quantum wells at vicinal Au(111) studied with angle-resolved photoemission. *Phys. Rev. B* **2002**, *66*, 245419.
 - [11] Ast, C. R.; Henk, J.; Ernst, A.; Moreschini, L.; Falub, M. C.; Pacilé, D.; Bruno, P.; Kern, K.; Grioni, M. Giant Spin Splitting through Surface Alloying. *Phys. Rev. Lett.* **2007**, *98*, 186807.
 - [12] Marchenko, D.; Varykhalov, A.; Scholz, M.; Bihlmayer, G.; Rashba, E.; Rybkin, A.; Shikin, A.; Rader, O. Giant Rashba splitting in graphene due to hybridization with gold. *Nature communications* **2012**, *3*, 1232.
 - [13] Zhang, X.; Liu, Q.; Luo, J.-W.; Freeman, A. J.; Zunger, A. Hidden spin polarization in inversion-symmetric bulk crystals. *Nature Physics* **2014**, *10*, 387–393.
 - [14] Ishizaka, K.; Bahramy, M.; Murakawa, H.; Sakano, M.; Shimojima, T.; Sonobe, T.; Koizumi, K.; Shin, S.; Miyahara, H.; Kimura, A.; others Giant Rashba-type spin splitting in bulk BiTeI. *Nature materials* **2011**, *10*, 521–526.
 - [15] Bahramy, M.; Arita, R.; Nagaosa, N. Origin of giant bulk Rashba splitting: Application to BiTeI. *Physical Review B—Condensed Matter and Materials Physics* **2011**, *84*, 041202.
 - [16] Di Sante, D.; Barone, P.; Bertacco, R.; Picozzi, S. Electric Control of the Giant Rashba Effect in Bulk GeTe. *Advanced Materials* **2013**, *25*, 509–513.
 - [17] Zhai, Y.; Baniya, S.; Zhang, C.; Li, J.; Haney, P.; Sheng, C.-X.; Ehrenfreund, E.; Vardeny, Z. V. Giant Rashba splitting in 2D organic-inorganic halide per-

- ovskites measured by transient spectroscopies. *Science Advances* **2017**, *3*, e1700704.
- [18] Wang, L.; Wesselink, R.; Liu, Y.; Yuan, Z.; Xia, K.; Kelly, P. J. Giant room temperature interface spin Hall and inverse spin Hall effects. *Physical review letters* **2016**, *116*, 196602.
 - [19] Amin, V. P.; Zemen, J.; Stiles, M. D. Interface-generated spin currents. *Physical review letters* **2018**, *121*, 136805.
 - [20] Miron, I. M.; Garello, K.; Gaudin, G.; Zermatten, P.-J.; Costache, M. V.; Auffret, S.; Bandiera, S.; Rodmacq, B.; Schuhl, A.; Gambardella, P. Perpendicular switching of a single ferromagnetic layer induced by in-plane current injection. *Nature* **2011**, *476*, 189–193.
 - [21] Lee, S.-W.; Lee, K.-J. Emerging three-terminal magnetic memory devices. *Proceedings of the IEEE* **2016**, *104*, 1831–1843.
 - [22] Ham, W. S.; Ho, T. H.; Shiota, Y.; Iino, T.; Ando, F.; Ikebuchi, T.; Kotani, Y.; Nakamura, T.; Kan, D.; Shimakawa, Y.; others Bulk Rashba-Type Spin Splitting in Non-Centrosymmetric Artificial Superlattices. *Advanced Science* **2023**, *10*, 2206800.
 - [23] Maji, T. K.; Kumbhakar, S.; Tongbram, B.; Sai, T. P.; Islam, S.; Mahapatra, P. S.; Pandey, A.; Ghosh, A. Electrical Resistance in a Composite of Ultra-Small Silver Nanoparticles Embedded in Gold Nanostructures: Implications for Interface-Enabled Functionality. *ACS Applied Electronic Materials* **2023**, *5*, 2893–2901.
 - [24] Kumbhakar, S.; Maji, T. K.; Tongbram, B.; Mandal, S.; Soundararaj, S. H.; Debnath, B.; Jain, M.; Krishnamurthy, H.; Pandey, A.; Ghosh, A. Engineering ultra-strong electron-phonon coupling and nonclassical electron transport in crystalline gold with nanoscale interfaces. *Nature Communications* **2025**, *16*, 61.
 - [25] Mandal, S.; Soundararaj, S. H.; Jain, M.; Krishnamurthy, H. R. Possibilities for enhanced electron-phonon interactions and high- T_c superconductivity in engineered bimetallic nanostructured superlattices. *Phys. Rev. B* **2025**, *111*, 184507.
 - [26] Bose, D.; Bakshi, S. S.; Majumdar, P. Enormous enhancement of resistivity in nanostructured electron-phonon systems. *2024*.
 - [27] Ziman, J. *Electrons and Phonons: The Theory of Transport Phenomena in Solids*; Oxford University Press, 2001.
 - [28] Bergmann, G. Inelastic life-time of the conduction electrons in some noble metal films. *Zeitschrift für Physik B Condensed Matter* **1982**, *48*, 5–16.
 - [29] Maekawa, S.; Fukuyama, H. Magnetoresistance in Two-Dimensional Disordered Systems: Effects of Zeeman Splitting and Spin-Orbit Scattering. *Journal of the Physical Society of Japan* **1981**, *50*, 2516–2524.
 - [30] Bergmann, G. Weak localization in thin films: a time-of-flight experiment with conduction electrons. *Physics Reports* **1984**, *107*, 1–58.
 - [31] Fukuyama, H.; Hoshino, K. Effect of Spin-Orbit Interaction on Magnetoresistance in the Weakly Localized Regime of Three-Dimensional Disordered Systems. *Journal of the Physical Society of Japan* **1981**, *50*, 2131–2132.
 - [32] Baxter, D. V.; Richter, R.; Trudeau, M.; Cochrane, R.; Strom-Olsen, J. Fitting to magnetoresistance under weak localization in three dimensions. *Journal de Physique* **1989**, *50*, 1673–1688.
 - [33] Browne, A. J.; Krajewska, A.; Gibbs, A. S. Quantum materials with strong spin-orbit coupling: challenges and opportunities for materials chemists. *Journal of Materials Chemistry C* **2021**, *9*, 11640–11654.
 - [34] Lee, P. A.; Ramakrishnan, T. V. Disordered electronic systems. *Rev. Mod. Phys.* **1985**, *57*, 287–337.
 - [35] Efros, A. L.; Pollak, M. *Electron-electron interactions in disordered systems*; Elsevier, 2012.
 - [36] Lu, H.-Z.; Shen, S.-Q. Weak localization and weak anti-localization in topological insulators. *Spintronics VII*. 2014; p 91672E.
 - [37] Jobst, J.; Waldmann, D.; Gornyi, I. V.; Mirlin, A. D.; Weber, H. B. Electron-Electron Interaction in the Magnetoresistance of Graphene. *Phys. Rev. Lett.* **2012**, *108*, 106601.
 - [38] Dey, R.; Pramanik, T.; Roy, A.; Rai, A.; Guchhait, S.; Sonde, S.; Movva, H. C.; Colombo, L.; Register, L. F.; Banerjee, S. K. Strong spin-orbit coupling and Zeeman spin splitting in angle dependent magnetoresistance of Bi₂Te₃. *Applied Physics Letters* **2014**, *104*.
 - [39] Elliott, R. J. Theory of the Effect of Spin-Orbit Coupling on Magnetic Resonance in Some Semiconductors. *Phys. Rev.* **1954**, *96*, 266–279.
 - [40] Yafet, Y. In *g Factors and Spin-Lattice Relaxation of Conduction Electrons***Part of the work connected with the preparation of this article, in particular the work on spin-lattice relaxation, was done while the author was at the Westinghouse Research Laboratories, Pittsburgh, Pennsylvania.; Seitz, F., Turnbull, D., Eds.; Solid State Physics; Academic Press, 1963; Vol. 14; pp 1–98.
 - [41] Dyakonov, M.; Perel, V. Current-induced spin orientation of electrons in semiconductors. *Physics Letters A* **1971**, *35*, 459–460.
 - [42] Dyakonov, M.; Perel, V. Spin relaxation of conduction electrons in noncentrosymmetric semiconductors. *Soviet Physics Solid State, Ussr* **1972**, *13*, 3023–3026.
 - [43] Nuber, A.; Braun, J.; Forster, F.; Minár, J.; Reinert, F.; Ebert, H. Surface versus bulk contributions to the Rashba splitting in surface systems. *Phys. Rev. B* **2011**, *83*, 165401.
 - [44] Reinert, F.; Nicolay, G.; Schmidt, S.; Ehm, D.; Hufner, S. Direct measurements of the L-gap surface states on the (111) face of noble metals by photoelectron spectroscopy. *Phys. Rev. B* **2001**, *63*, 115415.
 - [45] Nicolay, G.; Reinert, F.; Hufner, S.; Blaha, P. Spin-orbit splitting of the L-gap surface state on Au(111) and Ag(111). *Phys. Rev. B* **2001**, *65*, 033407.
 - [46] Tamai, A.; Meevasana, W.; King, P. D. C.; Nicholson, C. W.; de la Torre, A.; Rozbicki, E.; Baumberger, F. Spin-orbit splitting of the Shockley surface state on Cu(111). *Phys. Rev. B* **2013**, *87*, 075113.
 - [47] Petersen, L.; Hedegård, P. A simple tight-binding model of spin-orbit splitting of sp-derived surface states. *Surface Science* **2000**, *459*, 49–56.
 - [48] Bihlmayer, G.; Koroteev, Y.; Echenique, P.; Chulkov, E.; Blügel, S. The Rashba-effect at metallic surfaces. *Surface Science* **2006**, *600*, 3888–3891, Berlin, Germany: 4–9 September 2005.
 - [49] Ishida, H. Rashba spin splitting of Shockley surface states on semi-infinite crystals. *Phys. Rev. B* **2014**, *90*, 235422.
 - [50] Nagano, M.; Kodama, A.; Shishidou, T.; Oguchi, T. A first-principles study on the Rashba effect in surface systems. *Journal of Physics: Condensed Matter* **2009**, *21*, 064239.
 - [51] Shanavas, K. V.; Satpathy, S. Electric Field Tuning of the Rashba Effect in the Polar Perovskite Structures. *Phys.*

Rev. Lett. **2014**, *112*, 086802.

- [52] Naidyuk, Y. G.; Yanson, I. K. *Point-contact spectroscopy*; Springer Science & Business Media, 2005; Vol. 145.
- [53] Celiberti, L.; Fiore Mosca, D.; Allodi, G.; Pourovskii, L. V.; Tassetti, A.; Forino, P. C.; Cong, R.; Garcia, E.; Tran, P. M.; De Renzi, R.; others Spin-orbital Jahn-Teller bipolarons. *Nature Communications* **2024**, *15*, 2429.

AUTHOR CONTRIBUTIONS

S.K. and B.D. contributed equally to this work.

S.K., B.D., and A.G. conceived the idea. S.K., T.K.M., B.D., and A.G. designed and carried out the magnetotransport experiments with help from T.P.S. . S.K., T.P.S., and A.G. designed and performed the tunnelling experiments. T.K.M., S.K., and B.D. fabricated and characterized the samples. B.T performed the Transmission Microscopy measurements. S.M., M.J., and H.R.K. performed theoretical modelling. T.V.R. provided theoretical inputs. A.P. provided experimental inputs to the sample fabrication and contributed during the revision of the manuscript. S.K. and B.D. analysed the data. S.K., B.D., and A.G. wrote the manuscript with inputs from all the authors.

FUNDING

S.K. acknowledges support from the Prime Minister's Research Fellowship (PMRF). T.K.M. acknowledges the National Postdoctoral Fellowship (NPDF) for funding. B.T. acknowledges the Department of Science and Technology, Government of India, through the INSPIRE Faculty Fellowship (DST/INSPIRE/04/002484). S.M., M.J., and H.R.K. thank the Supercomputer Education and Research Centre (SERC) at the Indian Institute of Science (IISc) for providing the computational resources. M.J. acknowledges the National Supercomputing Mission of the Department of Science and Technology, India, and Nano Mission of the Department of Science and Technology for financial support under Grants No. DST/NSM/R&D_HPC_Applications/2021/23 and No. DST/NM/TUE/QM-10/2019 respectively. H. R. K. gratefully acknowledges support from the Indian National Science Academy under grant number No. INSA/SP/SS/2023/, the Science and Engineering Research Board of the Department of Science and Technology, India, under grant No. SB/DF/005/2017/, and at the International Centre for Theoretical Sciences (ICTS) from the Simons Foundation (Grant No. 677895, R.G.). A.P. acknowledges the IISc Institute of Eminence (IOE) for funding and support.